Experimental Characterization of an Electric Ducted Fan for the SUSAN 25% Scale Research Vehicle

Rose Weinstein* and Benjamin M. Simmons†
NASA Langley Research Center, Hampton, Virginia, 23681

An electric ducted fan (EDF) was tested in the NASA Langley 12-Foot Low-Speed Tunnel for the SUbsonic Single Aft eNgine (SUSAN) Electrofan 25% scale research vehicle, which incorporates distributed electric fans along the wings and serves as a scaled electrified transport aircraft testbed. The commercial-off-the-shelf EDF was selected as a propulsor that can meet the 25% scale vehicle geometry constraints, along with the performance requirements throughout the flight profile. The test included a series of one-factor-at-a-time (OFAT) and design of experiments (DOE) approaches that were implemented across a range of fan speed, voltage, freestream dynamic pressure, and incidence angle settings to characterize the performance of the EDF. Several test matrix designs and modeling approaches were considered. System identification methods were used to develop a static motor model, a dynamic motor model, an EDF thrust model, and a power consumption model. The model predictive capabilities were then evaluated with validation data not used in the modeling process. The results provide a comprehensive set of models developed to characterize the fan, and offer general insight into EDF modeling approaches.

I. Nomenclature

c	=	fan blade chord length, ft
C_P	=	fan power coefficient
C_T	=	fan thrust coefficient
D	=	fan diameter, ft
i_p	=	fan incidence angle, rad or deg
J	=	advance ratio
J_x	=	normal advance ratio
J_z	=	tangential advance ratio
n	=	fan rotational speed, rev/s
M_{tip}	=	fan tip Mach number
P	=	input power, W or kW
$\bar{q}$	=	dynamic pressure, psf
R^2	=	coefficient of determination
Re	=	fan Reynolds number
T	=	thrust, lbf
U	=	operating voltage, V
V	=	freestream velocity, ft/s
η	=	motor pulse width modulation command

Subscripts

$_0$	=	reference or bias value

Superscripts

$\hat{}$	=	estimate
$\bar{}$	=	mean

*Research Aerospace Engineer, Flight Dynamics Branch, AIAA Member.
†Research Aerospace Engineer, Flight Dynamics Branch, AIAA Member.

II. Introduction

The growing demand for sustainable air travel has led to a proliferation of technologies aimed at reducing emissions and improving aircraft operational efficiency. In recent years, there has been growing interest at NASA to invest in and explore the use of electrified aircraft propulsion (EAP) for environmental sustainability, with emerging aviation concepts including the Single-aisle Turboelectric AiRcraft with an Aft Boundary-Layer propulsor (STARC-ABL) and N3-X that utilize turboelectric propulsion along with other emerging technologies to reach emission goals [1, 2]. Within the NASA Aeronautics Research Mission Directorate (ARMD) Convergent Aeronautics Solutions (CAS) project, the SUbsonic Single Aft eNgine (SUSAN) Electrofan transport concept merges several new techniques in an EAP system aiming to reduce emissions by 50% while maintaining the size, speed, and range of single-aisle commercial transport aircraft [3, 4]. An ongoing trade study is exploring a wide range of novel airframe and propulsion designs that will enable favorable propulsion airframe integration (PAI) within SUSAN, and concurrent efforts are pursuing a propulsion, flight control, and power control architecture that leverages these advantages [3–9].

One of the key technologies considered by the SUSAN concept to enable PAI is distributed electric propulsion (DEP). Whereas the need for increased thrust and propulsive efficiency has traditionally led to larger diameter engines that have ground clearance and structural integration challenges, DEP instead distributes the required thrust across several smaller propulsive units, resulting in a higher effective bypass ratio of the propulsion system [10]. A DEP approach offers numerous potential advantages, such as a higher total capture area, and subsequent propulsive efficiency improvements; allowance for flexible and strategic fan placement; aero-propulsive interactions to be favorably leveraged, such as through boundary layer ingestion (BLI); and propulsion-based control allocation, which could reduce the need for control surfaces and decrease the size of the vertical tail. These benefits must also be balanced with the tradeoffs of structural integration challenges, increased drag, electric power requirements, and added noise [4, 10–12].

The SUSAN concept, shown in Fig. 1, employs a hybrid electric propulsion system with a single rear-mounted fuel-burning turbofan, which supports generators that supply power to 16 electric ducted fans (EDFs) distributed along the wing [5, 7]. The aft engine provides 35% of the total thrust, while the wing-mounted distributed propulsors collectively provide the remaining 65% [7].

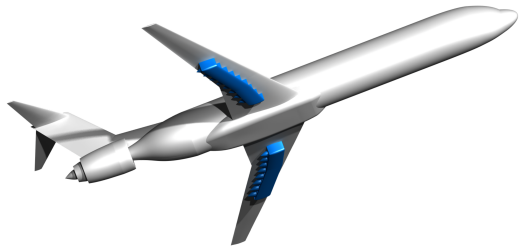

Fig. 1 SUSAN concept with DEP units along the wing.

Within the conceptual SUSAN trade study, there is an ongoing effort to develop a 25% scale vehicle to enable the experimental research, demonstration, and evaluation of key technologies within the integrated airframe, power, and propulsion system. The 25% scale testbed will allow flight-based research across the entire system architecture design, as well as the development and testing of flight, propulsion, and power controls.

This work focuses on the characterization and evaluation of the isolated wing-mounted distributed electric propulsion unit for the SUSAN 25% scale vehicle. The propulsion system considered in this paper is a commercial-off-the-shelf (COTS) EDF, motor, and electronic speed control (ESC), designated EDF v1. The objective of this work is first to develop the infrastructure to perform rapid ground-based bench tests and wind tunnel tests to efficiently study EDF performance, and then to characterize the EDF v1 by developing a static motor model, a dynamic motor model, a fan thrust model, and a power consumption model. These models will then be used to evaluate the EDF system suitability for the 25% scale vehicle.

This paper is organized as follows: Section III provides background and a summary of the literature reviewed for EDF empirical modeling. Section IV describes the EDF v1 components, the wind tunnel test setup, and the data acquisition for the experiment. Section V describes the modeling methods used in this work. Section VI presents the static motor, dynamic motor, thrust, and power consumption modeling results. In Sec. VII, thermal considerations for EDF operation are discussed, and in Sec. VIII, the EDF performance is assessed with regards to its suitability for the 25% scale vehicle. Finally, Sec. IX presents a summary and conclusions for this work.

III. Background

Past work at the NASA Langley 12-Foot Low-Speed Tunnel demonstrated the experimental testing of isolated propellers for applications across a variety of test vehicles, including electric vertical takeoff and landing (eVTOL) aircraft and multirotors [13, 14]. Some of these tests used a design of experiments (DOE) approach to enable efficient data acquisition across several test factors [15]. This paper builds upon these tests and other past DOE work [16–19] to incorporate the experiment design and modeling approaches for EDFs.

Compared to propellers, EDFs offer several advantages that can be considered when selecting an appropriate propulsor for a particular vehicle design and flight regime. The ducts can allow for increased thrust for a given blade diameter, reduce blade tip losses, shield noise propagation, and protect the surroundings from the blades, and vice versa [20]. Stators, or outlet guide vanes (OGVs), are utilized to connect the duct to the motor, and can also be designed to increase thrust with cambered airfoil shapes, and reduce swirl loss by straightening the efflux and reducing the overall net torque. EDFs provide additional options for acoustic treatments such as with liners or strategic stator designs, which are particularly relevant for SUSAN to meet FAA acoustic standards in the transport aircraft category [21]. EDFs tend to have smaller blade diameters compared to open rotors, which produce lower blade tip speeds for a given rotational speed, and therefore allow them to reach higher fan speeds. EDFs can also be used to operate at much higher airspeeds than propellers.

Some disadvantages of EDFs include the added complexity of manufacturing the ducted design to achieve desired performance, as well as the increased weight and structural integration challenges. It is also important to minimize the spacing between the blade and the duct to achieve the advantages of EDFs, but also to ensure it is wide enough to avoid friction and damage to both components. Finally, for the same thrust generated by a smaller diameter compared to a larger diameter rotor, the energy requirement is higher.

The approach to characterizing EDFs is similar to that of propellers, with a few considerations that set them apart, such as higher fan speeds, corresponding greater input power requirements, and close to zero net torque, which differs from propeller model development and efficiency computations.

Similar to propellers [14, 15], fan aerodynamics are often characterized as nondimensional variables that scale with density, motor speed, and blade diameter. The thrust and power coefficients are defined as

$$C_T = \frac{T}{\rho n^2 D^4}, \quad C_P = \frac{P}{\rho n^3 D^5} \tag{1}$$

These coefficients are generally modeled as a function of propeller advance ratio J, tip Mach number M_{tip}, and blade Reynolds number Re as

$$J = \frac{V}{nD}, \quad M_{\text{tip}} = \frac{\pi n D}{a}, \quad Re = \frac{\rho V_p c}{\mu} \tag{2}$$

where a is the speed of sound, c is the blade chord length at 75% of the blade diameter, μ is the dynamic viscosity, and $V_p = 0.75\pi nD$ is the blade speed at the 75% diameter location. EDF aerodynamics are most strongly a function of J, where a large magnitude represents a slow-rotating fan blade or a fast-moving vehicle, and a small number indicates a fast-rotating blade or a slow-moving vehicle. For blades that have a high rotational speed, the M_{tip} term represents the compressibility effects on the propeller blades. Reynolds number is the ratio of inertial forces to viscous forces experienced by the fan blade, and represents the relative impact of each of these contributions to the flow characteristics.

EDF performance is affected by the angle between the thrust vector and the freestream velocity, or the incidence angle i_p. For EDFs at incidence in flight that are exposed to both a normal component and a tangential component of freestream velocity, as shown in Fig. 2, the advance ratio can be expressed in terms of the components aligned parallel and perpendicular to the freestream velocity as [14]

$$J_x = \frac{V \cos i_p}{nD} = J \cos i_p, \quad J_z = \frac{V \sin i_p}{nD} = J \sin i_p \tag{3}$$

The wind-off efficiency of the EDF is evaluated using the figure of merit (FM) as [22–24]

$$\text{FM} = \sqrt{\frac{2}{\pi}} \frac{C_T^{3/2}}{C_p} \tag{4}$$

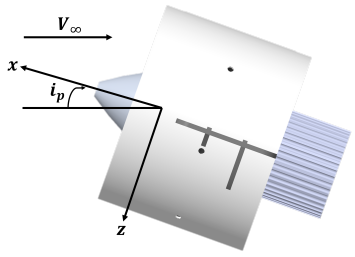

Fig. 2 EDF coordinate system and incidence angle.

IV. Experimental Setup

This section describes how the conceptual full-scale SUSAN EDF and the required thrust and available onboard power for the 25% scale vehicle led to the selection of the EDF v1 hardware. The 12-Foot Low-Speed Tunnel experimental setup is also discussed, including the instrumentation and the data streams available.

A. EDF Hardware Selection

The conceptual full-scale SUSAN aircraft has a 118 ft wingspan, with 16 EDFs mounted along the wing, each with a blade diameter of about 2.5 ft [5, 7]. Although precise geometric matching of each component of the full-scale concept to the 25% scale vehicle was not essential, selecting a COTS EDF with close to a 25% scaled blade diameter was desired to have an approximate geometrically scaled EDF.

The 25% scale vehicle is currently projected to weigh 1850 lb, with 35% of the total thrust provided by the rear-mounted engine, and 65% delivered from the wing-mounted propulsors. Assuming a thrust to weight ratio of 0.31 (for SUSAN baseline comparison to a Boeing 737-800 [25, 26]), each fan must provide 23 lbf of thrust. The necessary thrust estimates will be refined as the vehicle design and performance requirements mature, and further EDF versions will consider those aspects [27].

The onboard power distribution system for this vehicle extracts power from an internal combustion engine through a set of generators, with rechargeable batteries available as a backup power source. The constant operating voltage supplied by the power bus to the EDFs is 75 V; this will diminish to 50 V over time if operating on battery backup power. The generator will provide 150 kW of power, so with an estimated efficiency of 90%, each EDF has 8.5 kW of accessible power, considering all fans are running at maximum power. If the EDFs are used for differential thrust for vehicle control, then each fan can access additional power up to the total available bus power.

With these specified geometry, thrust, and power criteria, an initial inquiry into available COTS hardware led to the selection of the Jetfan 130 Pro EDF Unit, shown in Fig. 3, with fan design attributes summarized in Table 1. The EDF was purchased with a COTS inlet ring to improve inlet flow characteristics and fan efficiency, and is outfitted with an aluminum motor heat sink as shown. The EDF was dynamically balanced by the supplier prior to testing.

The Jetfan manufacturer provided sample bench test thrust data which showed that a TFL-56104 550 Kv motor could provide 23.3 lbf of static thrust with 6.97 kW of applied power with a 14S (14-cell) battery. Because the 25% scale vehicle supplies power with an 18S (18-cell) battery, it was expected that a 428 Kv motor would provide comparable thrust with the same total power, but with a lower current draw. The TFL SSS 56114 500 Kv inrunner brushless DC (BLDC) motor was therefore selected as the closest comparable motor, with the physical and performance attributes summarized in Table 2.

The ESC receives a throttle command, and converts a DC power source into an AC signal to turn the motor at a specified speed. The ESC had to be carefully selected to be compatible with the 18S power requirements, which led to the selection of the Advanced Power Drives (APD) UHV 20S ESC with an 85 V and 400 A continuous limit. The APD ESC is supplied by the manufacturer with an optional 120 V, 3600 μF capacitor bank which was used during the testing to mitigate voltage ripple and improve signal quality for extended DC power wire lengths necessary in the wind tunnel setup. The ESC accepts a standard pulse width modulation (PWM) input command η, which is a rectangular wave with a pulse width that is modulated to describe the throttle setting, where $\eta = 1100$ μs corresponds to a throttle at 0%, and 1900 μs designates a throttle setting of 100%. The ESC also transmits several data streams, which are summarized in Table 3, through the universal asynchronous receiver-transmitter (UART) output pins. An Arduino

Mega was programmed and used as the interface both to send the commanded PWM signals to the ESC from the data acquisition system (DAS), as well as to transmit the UART data back to the DAS to be recorded during testing. ESC data were streamed at 50 Hz, with time history as well as time averaged data recorded.

Fig. 3 Jetfan 130 Pro EDF unit and motor.

Table 1 Jetfan 130 Pro EDF attributes

Property	Value
Number of blades	10
Number of stators	7
Outer duct diameter	5.23 in
Blade diameter	5.11 in
Tip chord length	1.04 in

Table 2 TFL SSS 500 Kv motor attributes

Property	Value
Kv	500 rpm/V
Maximum voltage	90 V
Maximum current	132 A
Maximum continuous power	7 kW
Maximum rotational speed	45K rpm
Shaft diameter	10 mm
Poles	6
Mass	1100 g
Diameter	56 mm
Shaft length	30 mm

Table 3 ESC UART data

Signal	Unit
Rotational speed	rpm
Temperature	°C
Voltage	V
Current	A
Motor duty	%
Throttle duty	%

B. Wind Tunnel Setup and Instrumentation

The EDF characterization was conducted in the NASA Langley 12-Foot Low-Speed Tunnel,* which is an atmospheric pressure, closed return tunnel with a 12 ft octagonal test section. The dynamic pressure can be manually set from the control room, whereas the sting position and fan speed can be automatically controlled through the DAS, corresponding to each test point assignment.

A six-component strain gage balance was placed on the sting and connected to a bracket and clamp structure to support the EDF, as shown in Fig. 4a. During the test, the sting was rotated in the horizontal plane to adjust the EDF incidence angle, as displayed in Fig. 4b. The analog channels including balance forces and moments; tunnel parameters such as dynamic pressure, atmospheric pressure, and tunnel temperature; and sting incidence angle were recorded at 2500 Hz for each test point to allow for detection of the fan rotational frequencies in the balance measurements.

A TDK Genesys power supply, which offers a maximum of 80 V, 125 A, and 10 kW of power, was used to run the EDF up to a 75 V operating voltage. The power supply was programmed to set the applied voltage and current limits from the DAS, as well as to transmit voltage and current data at 2 Hz to the DAS to be recorded during the test.

*https://researchdirectorate.larc.nasa.gov/12-foot-low-speed-tunnel-12-ft-lst/

(a) Front view of EDF mounted to the sting **(b) Top view of sting with EDF at an incidence angle**

Fig. 4 Experimental setup in NASA Langley 12-Foot Low-Speed Tunnel.

C. Experiment Design

One-factor-at-a-time (OFAT) runs were initially performed to explore the test factor ranges and provide a preliminary understanding of the variation of the response variables as a function of each test factor. An approach employing DOE and response surface methodology (RSM) [28, 29] was then applied to develop efficient test matrices that varied up to four test factors: dynamic pressure $\bar{q}$, incidence angle i_p, PWM command η, and operating voltage U. The term "DOE" used henceforth in the paper should be interpreted to also include "RSM." The statistical experiment design approach was formulated based on practical operational considerations. Dynamic pressure and voltage were designated as hard-to-change (HTC) factors because they required manual, more time-consuming adjustment for this particular wind tunnel test. Incidence angle and PWM command were considered to be easy-to-change (ETC) factors because they could be commanded quickly and automatically through the DAS.

Due to the presence of HTC and ETC factors, response surface designs that include restricted randomization for HTC factors, referred to as split-plot designs [30, 31], were applied for this study. Split-plot designs are used to conduct efficient experiments with HTC factors, while still executing a statistically-rigorous designed experiment. The HTC factors are held at a constant value for several consecutive test points while the ETC factors are varied between each test point. The different amount of randomization for HTC factors and ETC factors results in different variance components, which must be considered for experiment design and data analysis [29]. The designs applied for this work were split-plot I-optimal response surface designs created using Design-Expert®, a commercially available statistical software package [32]. I-optimal designs minimize the integrated prediction variance for a design model structure over the range of test factors [28, 29]. Each DOE test matrix consisted of a set of optimal modeling test points, center points to quantify the measurement noise at a repeated condition, and validation data withheld from the modeling process that were later used to assess the model predictive capability. The overall design strategy followed the approach presented in detail in Ref. [33]. Separate from Ref. [33], for this work, a new technique was implemented to incorporate linear constraints into the experiment design process. This was necessary to accommodate a maximum power constraint, which was implemented in the design by limiting the maximum PWM value as a linear function of operating voltage.

V. Modeling Approach

This section describes the parameter estimation and model structure determination processes that were implemented for model development throughout this work, along with key metrics used for model quality assessment. These methods were implemented from the software toolbox System IDentification Programs for AirCraft, or SIDPAC [34].

A. Model Identification for Time Averaged Data

For the models developed in this paper using time-averaged data, the parameters for each model were estimated by minimizing the equation error in the least-squares sense, with the ordinary least squares process described in detail in Ref. [34]. Throughout most of the equation-error models developed in this work, the explanatory variables were centered about the median values to retain the low correlation among candidate regressors that is achieved through the experiment design.

For each response variable, a pool of candidate polynomial model terms was postulated up to a specified maximum model term order using physical insight into the relevant terms that might be needed to adequately model the response variables, and based upon the maximum model order permitted by the experiment design. The particular regressors for each model were then chosen based on a multivariate orthogonal function (MOF) model structure determination process [34, 35].

As mentioned in Sec. IV.C, the DOE test matrices used for this study were obtained from split-plot designs [30, 31], or designs with restricted randomization for certain test factors. This results in a compound error structure with different whole-plot and sub-plot variance estimates. Generally, restricted maximum likelihood (REML) analysis is used to estimate the variance components and generalized least-squares is used for parameter estimation when developing models for split-plot experiments [36]. However, for this work, multivariate orthogonal function (MOF) modeling and ordinary least-squares regression were applied for model structure determination and parameter estimation for similar reasons to those that are explained and justified in Ref. [33].

B. Model Fit Metrics

After the modeling process has been completed, the effectiveness of the resulting model can be quantified by several modeling metrics. The coefficient of determination,

$$R^2 = 1 - \frac{\sum_{i=1}^{N}[z(i) - \hat{y}(i)]^2}{\sum_{i=1}^{N}[z(i) - \bar{z}]^2} \tag{5}$$

is a model fit quality measure that varies from 0 to 1 and describes how much of the variation in the data about the mean value is captured by the model, where z is the response variable to be modeled over N measurements, and $\hat{y}$ is the estimated model output.

Another metric used to evaluate the model quality was the normalized root-mean-square error (NRMSE), expressed as a percentage, and defined as

$$\text{NRMSE} = 100 \times \frac{1}{\text{range}(z)} \sqrt{\frac{1}{N}(z - \hat{y})^T (z - \hat{y})} \tag{6}$$

with $\text{range}(z) = z_{max} - z_{min}$ defined with response variable measurements used for model development. NRMSE provides a useful error quantification and a fair comparison between modeling and validation data, as discussed in Refs. [14, 37].

C. Model Identification for Dynamic Data

The dynamic motor model, which describes the transient response of the fan speed to the input command, was developed using output error parameter estimation. The output error method is a maximum likelihood parameter estimation approach that minimizes the sum of squared differences between the measured output data and the model output. The nonlinear cost function is solved iteratively using a modified Newton-Raphson method, and implemented with SIDPAC, with additional information in Ref. [34].

VI. Results

This section discusses the results obtained from the wind tunnel experiment, and how they were used to develop a static motor model, a dynamic motor model, a fan thrust model, and a power consumption model. A set of OFAT and DOE runs was performed across four test factors to collect static and dynamic motor data, EDF aerodynamic data, power consumption data, and thermal data, with the wind-off and wind-on runs summarized in Table 4. The test factors and corresponding ranges for the OFAT runs are shown in Table 5 and are briefly explained. The PWM input command spanned the full throttle range designated by the ESC, with the maximum allowed throttle a function of the operating voltage based on the motor power limit. The 25% scale vehicle onboard power distribution system provides 75 V to the EDF, so most runs were performed at this voltage. During a failure case of emergency loss of bus power, the EDFs would be powered by backup batteries onboard the vehicle, which would discharge from 75 V down to 50 V over time. To model the altered EDF performance in these circumstances, several runs were performed by varying the operating voltage across this range. The freestream dynamic pressure for the wind-on runs spanned from 0.25 to 6 psf to alter the

freestream velocity and vary advance ratio. Finally, the fan incidence angle relative to the oncoming flow was varied from 0 to 30 deg to span a wide range of angle-of-attack conditions that could be experienced in flight.

The OFAT runs were performed primarily for design space exploration and validation in wind-on and wind-off conditions, while the DOE runs efficiently covered the operational ranges of multiple test factors (designated with "F" as shorthand for "Factor") for global modeling. The 2F wind-off run varied η and U to explore the baseline fan performance with no freestream velocity component. For the wind-on runs, the 2F case varied the two primary factors of interest, η and $\bar{q}$, to characterize the fan as a function of J, while the 3F run added i_p, and the 4F run also included changes in U. Although the 4F run alone contains all factor variations across the 2F and 3F cases, each of these runs was performed to investigate the effect of the inclusion of each additional factor. The median values for explanatory variables used to develop the models in 2F Run 116 and 3F Run 97 are shown in Table 7 and Table 8, respectively, which will be used in the models as discussed in Section V.A.

Table 4 OFAT and DOE runs across four factors

Type	Factors	Run	PWM (μs)	Dynamic Pressure (psf)	Voltage (V)	Incidence Angle (deg)
OFAT	2F	117	[1150, 1765]	0	75	0
		118	[1150, 1825]		66.7	
		119	[1150, 1900]		58.4	
		120	[1150, 1900]		50	
DOE	2F	116	[1350, 1900]	0	[50,75]	0
OFAT	2F	107–114	[1150,1765]	0.25, 0.5, 1, 2, 3, 4, 5, 6	75	0
		80–82,84–88	[1150, 1825]		66.7	
		72–79	[1150, 1900]		50	
DOE	2F	94	[1350, 1765]	[0.25, 6]	75	0
DOE	3F	97	[1350, 1765]	[0.25, 6]	75	[0, 30]
DOE	4F	98	[1350, 1900]	[0.25, 6]	[50, 75]	[0, 30]

Table 5 Input test factor ranges for OFAT runs

Factor	Minimum	Maximum
PWM (μs)	1100	1900
Voltage (V)	50	75
Dynamic pressure (psf)	0	6
Incidence angle (deg)	0	30

Table 6 Measured or calculated output data for OFAT runs

Factor	Minimum	Maximum
Fan speed (rpm)	2,875	25,150
Static thrust (lbf)	0	21.25
Advance ratio	0.085	1.84
Power (W)	190	6,420

Table 7 Median explanatory variable values for 2F Run 116

Variable	Value
η (μs)	1603
U (V)	61.66
n (rev/s)	285.94

Table 8 Median explanatory variable values for 3F Run 97

Variable	Value
J_x	0.313
J_z	0.074
J	0.324
M_{tip}	0.374

A. OFAT Data

The OFAT runs enabled test envelope exploration in both wind-off and wind-on conditions, provided baseline data to inform best practices for the rest of the experiment, and offered insight into defining the most relevant DOE design space across each test factor. The ranges of measured or calculated output variables from the OFAT runs are summarized

in Table 6, and Fig. 5 displays OFAT results that will be discussed in detail next. All results are obtained at a 75 V operating voltage unless otherwise specified.

Figure 5a shows the measured fan speed as a function of the PWM command across wind-off conditions at each of four operating voltages, with a maximum of 25,150 rpm measured at 75 V. A PWM command of 1150 μs set the fan to an idle speed, and while the 58.4 V and 50 V runs reached the maximum throttle setting of 1900 μs, the 75 V and 66.7 V cases hit a lower PWM ceiling due to reaching the specified motor power limit. For the DOE runs with both PWM and voltage specified as test factors, these results provided insight for a design space constraint that defines the maximum PWM as a function of the voltage. This plot also indicates a nonlinear fan speed response at low PWM with this ESC, while the response above $\eta = 1350$ μs is more linear. Figure 5b similarly displays the fan speed response for wind-on conditions across the $\bar{q}$ range, and identifies a range of input commands for $\eta < 1350$ μs where windmilling occurs, such that the freestream velocity is increasing the fan speed beyond the speed that is controlled directly by the input power. The rotational speed for a given PWM command is approximately the same above $\eta = 1350$ μs, independent of $\bar{q}$.

The thrust generated as a function of fan speed is shown in Fig. 5c, with a maximum of 21.25 lbf of thrust measured in wind-off conditions, and a reduction in thrust as $\bar{q}$ increases. These thrust measurements, which are corrected to remove the effect of the bracket and adapter drag (as will be discussed in Section VI.B), appear to have a quadratic response character as a function of fan speed, as expected. There is also notably a range of low fan speed where the EDF drag exceeds the thrust generated; these are not useful, practical factor values to include in the DOE design. These negative thrust points can be observed more clearly in Fig. 5d, which shows C_T as a function of J at each $\bar{q}$ condition. The points above $J = 1.24$ are associated with a negative thrust measurement, and are considered impractical test points.

The variation of J across fan speed at different $\bar{q}$ values is shown in Fig. 5e. Although a large portion of the J range can be achieved at a single $\bar{q}$ condition, or within a smaller range of $\bar{q}$, the runs were performed across a wide range to decorrelate advance ratio effects from EDF rotational speed effects, which could be present in the form of both Reynolds number and tip Mach number effects.

The power drawn as a function of fan speed was shown to have a cubic response, as displayed in Fig. 5f, with a small reduction in power required at a higher $\bar{q}$. Given the steepness of the power curve at high fan speed and the implications for power fluctuations, as well as the high nominal operating voltage of 75 V, a maximum of $\eta = 1765$ μs corresponding to 6.4 kW in wind-off conditions was specified for the 75 V runs to remain conservative during extended testing. These results shown were extrapolated to the full 7 kW motor maximum continuous power setting, which resulted in a PWM command of 1779 μs, fan speed of 26,000 rpm, and thrust of 22.6 lbf, which are close to the maximum outputs measured in Table 6, indicating that only a limited range of test factors was excluded.

As discussed in Section III, EDFs are purposely designed with OGVs that remove the swirl from the fan efflux. The OGVs are airfoils whose net tangential forces, at a distance from the fan hub, produce a counter-torque that effectively zeros the torque that would otherwise be generated with an open propeller. This precludes traditional propeller efficiency approaches, particularly in wind-off conditions, which consider a ratio of mechanical rotational output power to electrical input power. Therefore, the figure of merit in Eq. (4) was used to evaluate the EDF performance in the wind-off condition, as displayed in Fig. 5g, with a maximum of 80% shown at high fan speed.

B. Bracket Drag Model

The bracket and clamp structure used to secure the EDF and attach it to the sting was connected to the metric side of the balance, and consequently added drag to the balance measurements with nonzero freestream velocity, which causes a reduction in apparent measured thrust produced by the EDF. A wind-on bracket "tare" was performed across the ranges of $\bar{q}$ and i_p to develop a model that could be used to predict the bracket drag to subtract from the fan thrust measurements. Because the thrust models were developed in the EDF body axes, only the x component of drag was modeled. Note that this approach assumes that the bracket drag can be decoupled from the EDF drag, and does not account for any interactions. Figure 6a shows the bracket and fan mounted to the balance during the experiment, and Fig. 6b shows the bracket during the wind-on tare.

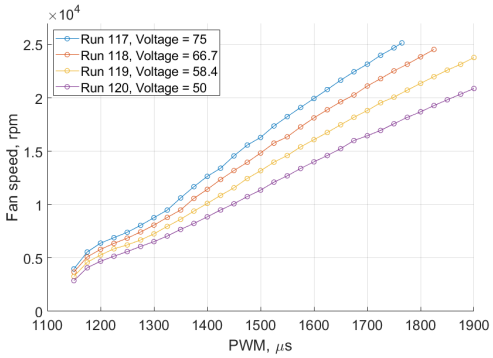

(a) Fan speed across PWM input with wind off

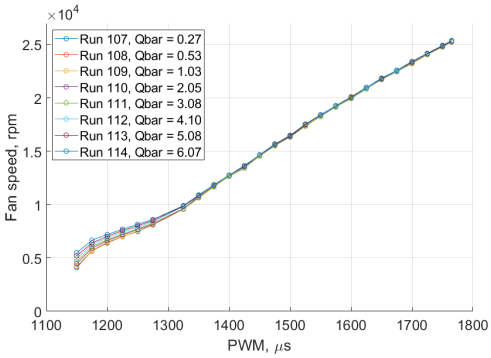

(b) Fan speed across PWM input with wind on

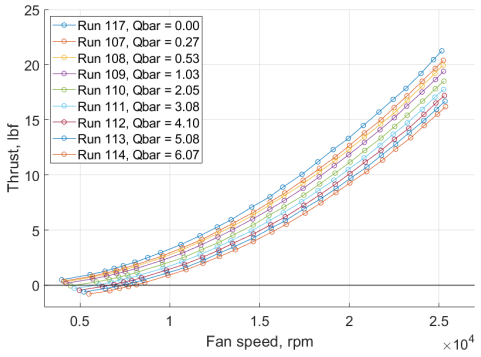

(c) Thrust generated across fan speed.

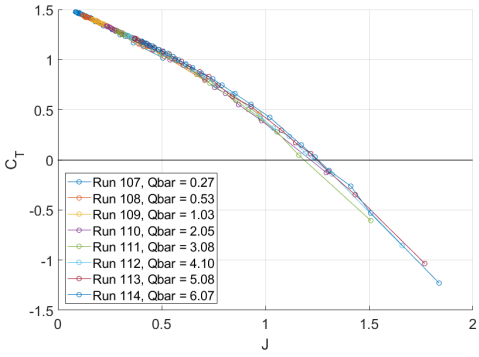

(d) Thrust coefficient across advance ratio

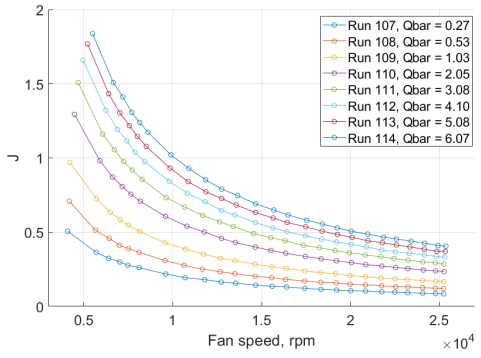

(e) Advance ratio across fan speed

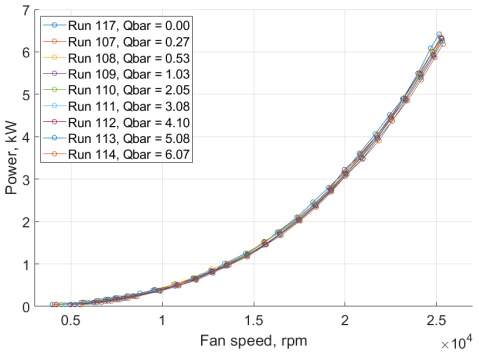

(f) Power consumption across fan speed

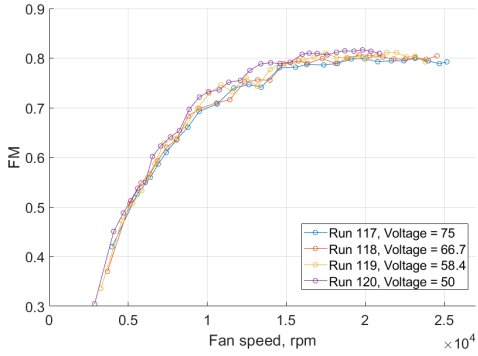

(g) Figure of merit across fan speed

Fig. 5 Wind-off and wind-on OFAT data.

(a) Nominal EDF runs

(b) Wind-on tare

Fig. 6 EDF bracket mounted to the balance.

A 2F DOE run was designed across $\bar{q}$ and i_p, with the bracket drag modeled as a function of these ordinary (uncentered) explanatory variables, which produced a more parsimonious model. The selected model structure was

$$X = X_0 + X_{\bar{q}}\bar{q} + X_{\bar{q}i_p^2}\bar{q}i_p^2 \tag{7}$$

with the parameter estimates and associated uncertainties presented in Table 9. This simple model structure characterizes the drag data well, with the modeling and validation data fit metrics given in Table 10, and the response surface shown in Fig. 7a, along with the modeling and validation data. An increase in $\bar{q}$ is seen to cause a strong increase in drag with up to 2 lbf measured around $\bar{q}$ = 6 psf, and maximum drag experienced at low i_p when the bracket is maximally exposed to the flow. Figure 7b shows the effect of the bracket drag model on the corrected thrust data at $\bar{q}$ = 0.27 and 6.07 psf at $i_p = 0$, with only a small difference in thrust seen at low $\bar{q}$, and a significant adjustment required at high $\bar{q}$. This drag correction expanded the range of useful fan speeds that generate positive thrust for experiment design purposes from what was initially observed during the exploratory runs.

Table 9 Bracket drag parameter estimates

Term	$\hat{\theta}$	$s(\hat{\theta})$	% Error
X_0	-3.442×10^{-2}	3.564×10^{-3}	10.4
$X_{\bar{q}}$	-3.208×10^{-1}	1.127×10^{-3}	0.4
$X_{\bar{q}i_p^2}$	1.425×10^{-1}	5.479×10^{-3}	3.8

Table 10 Bracket drag modeling and validation metrics

	R^2	NRMSE (%)
Model	0.999	0.683
Validation	0.999	0.622

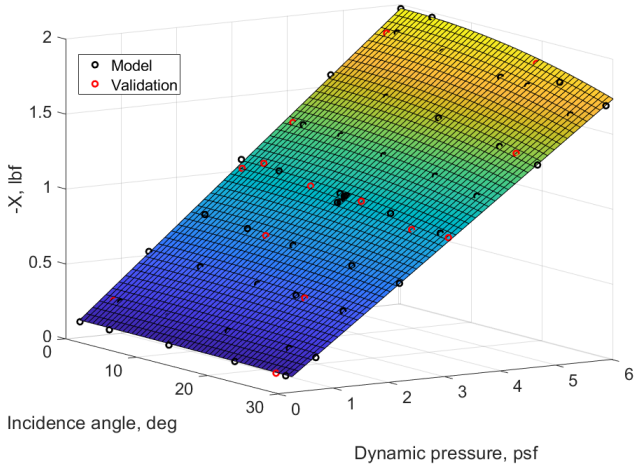

(a) Bracket drag response surface

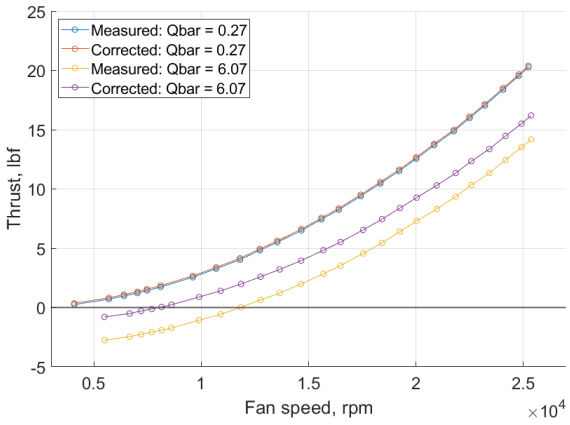

(b) Effect of bracket drag model on thrust data

Fig. 7 Bracket drag modeling results.

C. Static Motor Model

The static motor model describes the steady-state motor speed n, as a function of the PWM input command η, and voltage U. There were several elements that influenced the selection of the starting PWM command for the DOE design space, based on the insight provided in Sec. VI.A. First, Fig. 5a shows a nonlinear motor response up to $\eta = 1350$ μs for a constant voltage, and a mostly linear response beyond that point. Second, Fig. 5b shows an undesirable windmilling effect across that same range of η for the wind-on conditions. Figure 8 shows the effect of windmilling in more detail across the full range of $\bar{q}$ for the 75 V and 50 V OFAT runs. Because the 50 V case requires a larger value of η to achieve the same fan speed as the 75 V case, the windmilling effect can be seen across a wider range of η. For the 75 V case, the effect subsides at around $\eta = 1350$ μs. For the 50 V case it extends further in η, but since the 75 V nominal case is the main priority for this experiment, those runs were used to primarily drive the design space. Third, in Fig. 5c there is a range of fan speed inputs at higher $\bar{q}$ where the drag exceeds the thrust, which is also reflected in the negative C_T seen in Fig. 5d. Fourth, the ESC itself provides reliable fan speed feedback, and a closed loop fan speed controller will most likely be implemented, which reduces the direct relevance of the static motor model, particularly at low speeds where windmilling occurs. Fifth, and taking into account the aspects mentioned previously, there is a range of fan speed shown in Fig. 5c where this windmilling, nonlinear response behavior, and negative thrust occur, which provides minimal fan thrust compared to what is required in the cruise condition, and which would likely only be experienced briefly during engine run-up at takeoff. Finally, a coupled axial sting structural mode was identified during OFAT exploratory work at approximately 140 Hz (or 8,400 rpm) that was excited at $\eta = 1300$ μs for the 75 V case, and that was exacerbated at higher $\bar{q}$. All of the above considerations led to selecting a minimum of $\eta = 1350$ μs for the DOE runs, as listed in Table 4.

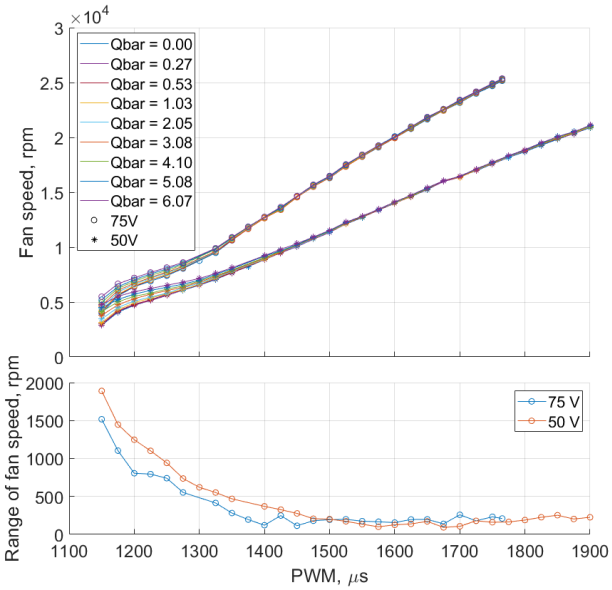

Fig. 8 Windmilling effect during wind-on conditions for 75 V and 50 V OFAT runs.

Two DOE runs were considered for the static motor model development: a wind-off 2F run, and a wind-on 4F run, with the measured test points across η and U shown in Fig. 9a for both runs. Note that a linear constraint was implemented in the design to limit the power draw at higher voltage.

The explanatory variables considered for the wind-off data included $n = f(\eta, U)$, while for the wind-on data, $n = f(\eta, U, V)$ to consider any airflow-induced changes in motor response. Although these conditions are outside of the main windmilling region, a small freestream velocity effect was still considered to be statistically included in the model structure. The ESC voltage reading was used in lieu of the power supply voltage since it detected a physically meaningful reduction in voltage as current increased, and more closely represented the motor response for a given ESC.

The model structure selected for both runs was

$$n = n_0 + n_\eta \eta + + n_U U + n_{\eta^2}\eta^2 + n_{\eta U}\eta U + n_{\eta^2 U}\eta^2 U \tag{8}$$

Note that for the 4F run, the effect of freestream velocity on motor response was insignificant, and no velocity terms were chosen in the model. The response surface for the 2F static motor model is shown in Fig. 9b, which indicates that higher η and U yield larger n, as expected. Although n was modeled in the units of rev/s, the results here are shown in units of rpm. The quantitative metrics for model fit were similar across both models, with the 2F model performing slightly better on both the modeling and validation data. Both static motor models were tested with OFAT validation data across variations in U and $\bar{q}$. Because the quantitative model fit metrics were similar for each model and the freestream velocity was not deemed significant for modeling the fan speed response, the 2F model was selected over the 4F model, with the model results provided in Tables 11 and 12. Note that the voltage factor only directly affects the static motor model, while the thrust and power models, which are based upon n, are not directly dependent on operating voltage.

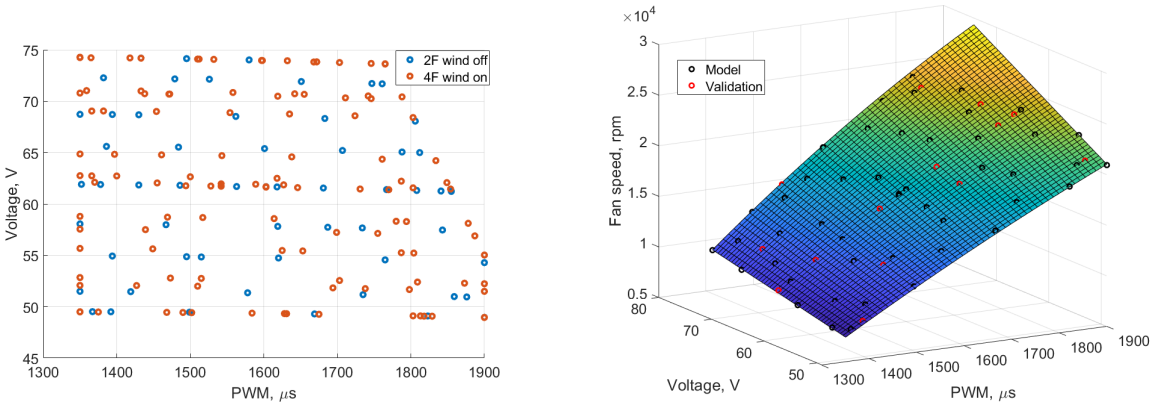

(a) Design space for static motor model

(b) Static motor response surface

Fig. 9 Static motor modeling results.

Table 11 Static motor model parameter estimates

Term	$\hat{\theta}$	$s(\hat{\theta})$	% Error
n_0	2.857×10^{2}	2.233×10^{-1}	0.1
n_η	4.962×10^{-1}	1.108×10^{-3}	0.2
n_U	4.005×10^{0}	3.224×10^{-2}	0.8
n_{η^2}	-1.480×10^{-4}	7.145×10^{-6}	4.8
$n_{\eta U}$	6.391×10^{-3}	1.275×10^{-4}	2.0
$n_{\eta^2 U}$	-4.676×10^{-6}	8.791×10^{-7}	18.8

Table 12 Static motor modeling and validation metrics

	R^2	NRMSE (%)
Model	1.000	0.375
Validation	1.000	0.376

D. Dynamic Motor Model

The dynamic motor model describes the transient response of the motor speed $n(t)$, as a temporal function of the input command $\eta(t)$. Data were gathered through η step commands with several factors varied including ramp rate, step direction, step size, initial condition, and freestream velocity, as shown in Table 13. The data sets used for modeling included a series of step commands across the range of η, with the step size and ESC ramp rate constant. For each ramp rate, a separate step command run was performed across each of the η step sizes, as shown for example in Fig. 11.

The data sets were parsed and each individual step response was extracted to develop a dynamic model at each of the combinations of various factors, and to determine which factors most strongly influence the response. Given the nature of the response, a first order dynamic model was initially considered, but the estimated time constants showed a consistently slower response than the data indicated, so a critically damped second order dynamic model was used, with the model structure chosen as

$$n(t) = n_0[1 - (1 + t/\tau_s)e^{t/\tau_s}] \tag{9}$$

Table 13 Dynamic motor experiment test factors

Factor	Values
ESC ramp rate	5%, 10%, 25%, 50%
Direction	increasing, decreasing
Step size (relative η)	25, 50, 100, 200
Initial condition (absolute η)	[1350, 1700]
Freestream velocity	off, 4 psf

The steady-state response term n_0 was predicted using the static motor model described in Section VI.C, and the second order time constant τ_s was optimized using the output error method. The resulting models were compared to establish the main influencing factors on the response time. The command direction, initial condition, and freestream velocity did not have a strong impact on the response, while the ESC ramp rate and step size strongly affected the dynamics, as shown in Fig. 12 for several ramp rates across each step size. It is apparent that the effect of ramp rate is dependent on $\Delta\eta$; for smaller $\Delta\eta$, there is no apparent difference in response time, while for higher $\Delta\eta$, the response with the larger ramp rate converges much faster. Additionally, the effect of $\Delta\eta$ on the response time is dependent on the ramp rate; at smaller ramp rates, there is a larger variation in response time as a function of $\Delta\eta$, while for larger ramp rates, the effect of $\Delta\eta$ is smaller.

Because the ESC ramp rate is a discrete setting that must be manually set, and is not varied in a particular run, a separate model for τ_s was developed for each ESC setting, as a function of $\Delta\eta$. Each step response in the staircase data set was modeled individually, and a weighted arithmetic mean was computed across the models for all of the absolute η commands at a given ramp rate and $\Delta\eta$, that takes into account multiple parameter estimates. A cubic model of τ_s was then developed for each ESC ramp rate, with the results in Fig. 10 showing that most of the ramp rates provide a similar response at low $\Delta\eta$, and that the effect of step size becomes less apparent at the higher ramp rates. The uncertainty estimates for each dynamic model were corrected for colored residuals, and then a weighted arithmetic mean was computed for the uncertainty at each point shown. Figure 11 shows the response data and dynamic model fit for a ramp rate of 5% with $\Delta\eta = 100$.

Although the higher ramp rates appear to provide both a faster and more uniform dynamic response across varying $\Delta\eta$, both of which are desirable for control applications, the tradeoff for higher ramp rate lies in the current spikes that result from rapid setpoint changes, with the time history of ESC current data shown in Fig. 13 for $\Delta\eta = 100$. The current for the 5% ramp rate gradually increases toward the steady-state level; in contrast, the higher ramp rates cause significant current spikes that could damage electronics and wiring if they not rated appropriately. The current spikes are also less severe for smaller step sizes, so several aspects need to be considered before selecting an acceptable ramp rate setting.

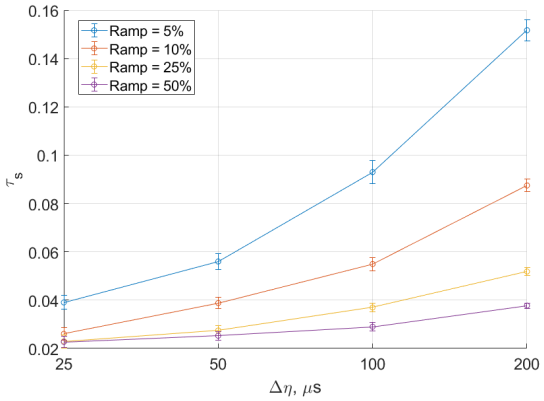

Fig. 10 Second order system parameter estimate for different ramp rates across each step size.

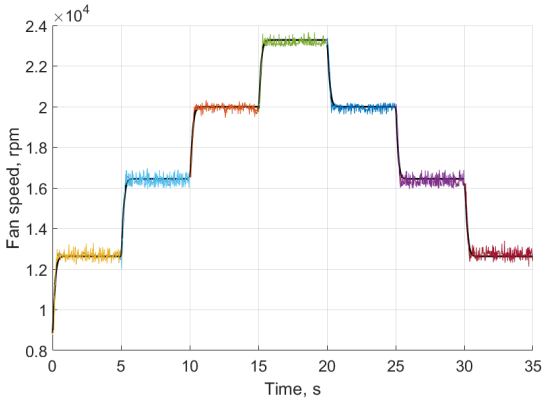

Fig. 11 Model fit for varying η step commands with $\Delta\eta = 100$ for an ESC ramp rate of 5%.

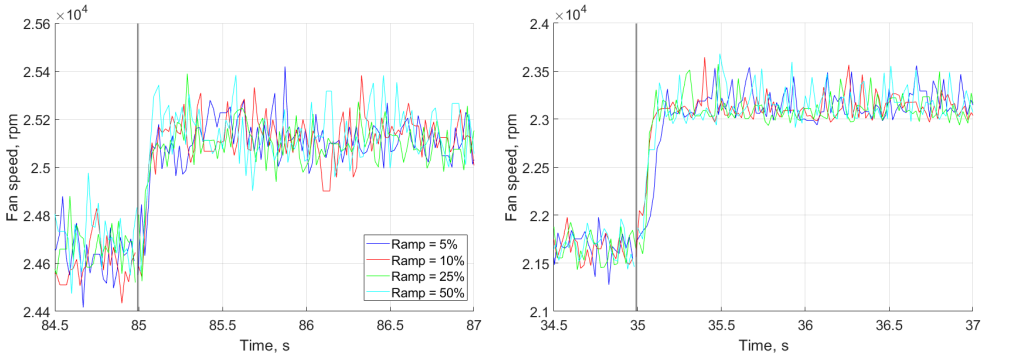

(a) $\Delta\eta$ = 25 μs **(b) $\Delta\eta$ = 50 μs**

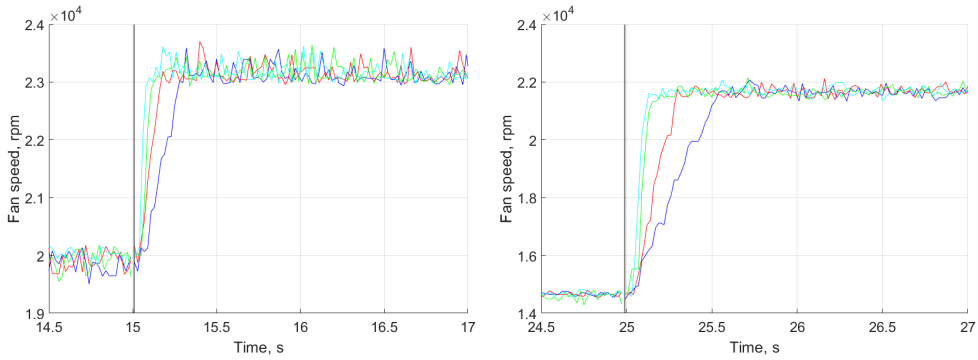

(c) $\Delta\eta$ = 100 μs **(d) $\Delta\eta$ = 200 μs**

Fig. 12 Dynamic response as a function of ESC ramp rate across varying η step sizes.

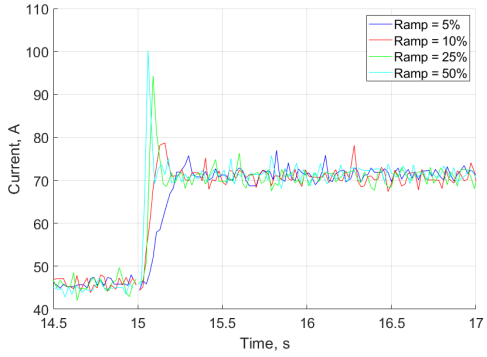

Fig. 13 ESC current measurements across ramp rate for $\Delta\eta$ = 100.

E. Wind-off EDF Performance

In contrast to propeller modeling for rotorcraft or eVTOL vehicles, there is no hover state for the EDFs used for a transport aircraft. Nevertheless, wind-off EDF characterization still provides a useful benchmark for rapid fan performance evaluation and comparison without a wind tunnel test, so wind-off fan thrust and power models were developed from the 2F DOE run.

Equation (1) presents expressions for thrust and power coefficients that describe a quadratic and cubic relationship between n and dimensional thrust and power, respectively. Accordingly, a second order thrust model

$$T = T_0 + T_n n + T_{n^2} n^2 \tag{10}$$

and a third order power model

$$P = P_0 + P_n n + P_{n^2} n^2 + P_{n^3} n^3 \tag{11}$$

were developed, with the parameter estimates provided in Tables 14 and 15. The prediction capabilities of these models were tested using validation data from the OFAT voltage runs, with the model fits and residuals shown in Fig. 14.

Table 14 Wind-off thrust model parameter estimates

Term	$\hat{\theta}$	$s(\hat{\theta})$	% error
T_0	9.806×10^{0}	7.870×10^{-3}	0.1
T_n	6.922×10^{-2}	7.678×10^{-5}	0.1
T_{n^2}	1.204×10^{-4}	8.994×10^{-7}	0.7

Table 15 Wind-off power model parameter estimates

Term	$\hat{\theta}$	$s(\hat{\theta})$	% error
P_0	1.998×10^{0}	4.485×10^{-3}	0.2
P_n	2.040×10^{-2}	1.005×10^{-4}	0.5
P_{n^2}	7.476×10^{-5}	5.507×10^{-7}	0.7
P_{n^3}	1.119×10^{-7}	7.229×10^{-9}	6.5

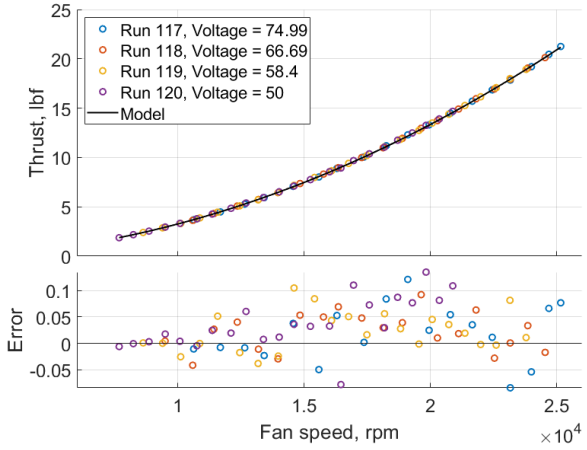

(a) Thrust model fit

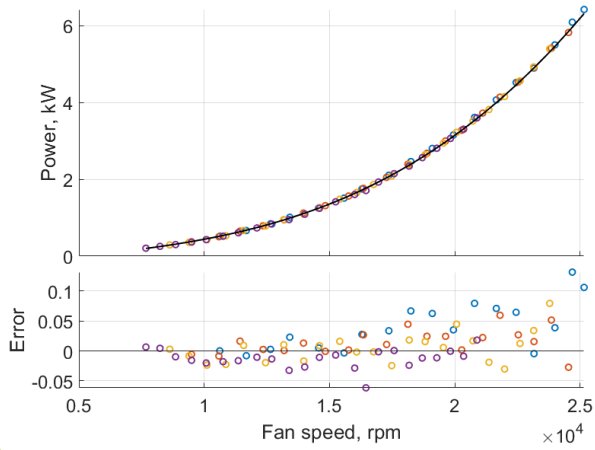

(b) Power model fit

Fig. 14 Wind-off thrust and power modeling results with OFAT validation data.

F. Thrust coefficient

The fan thrust model describes the nondimensional thrust coefficient C_T, with a separate C_T model developed using the DOE 2F, 3F, and 4F runs. Each of these models was compared to one another to evaluate the utility of the experiment designs.

The 2F run was performed across η and $\bar{q}$, with the thrust coefficient candidate explanatory variables including $C_T = f(J_x, M_{\text{tip}})$. For the high fan rotational speeds exhibited in this test, M_{tip} was considered as an explanatory variable instead of Re based on engineering judgment, as compressibility effects would be more apparent and Re effects more negligible. For the 3F and 4F runs, i_p was also included as a candidate explanatory variable, so $C_T = f(J_x, J_z, M_{\text{tip}})$. The selected model structure for the 2F model was

$$C_T = C_{T_0} + C_{T_{J_x}} J_x + C_{T_{J_x^2}} J_x^2 \tag{12}$$

the 3F model structure was

$$C_T = C_{T_0} + C_{T_{J_x}} J_x + C_{T_{J_z}} J_z + C_{T_{J_x M_{\text{tip}}}} J_x M_{\text{tip}} + C_{T_{J_x^2 M_{\text{tip}}}} J_x^2 M_{\text{tip}} \tag{13}$$

and the 4F model structure was

$$C_T = C_{T_0} + C_{T_{J_x}} J_x + C_{T_{J_z}} J_z + C_{T_{J_x M_{\text{tip}}}} J_x M_{\text{tip}} + C_{T_{J_z^2}} J_z^2 + C_{T_{J_x^2 M_{\text{tip}}}} J_x^2 M_{\text{tip}} \tag{14}$$

The 2F run provided an excellent model fit for the 75 V fan thrust data at $i_p = 0$, with a moderately degraded prediction for the 3F data, because it did not account for the effect of incidence angle that is addressed with the inclusion of both the J_x and J_z explanatory variables, as shown in Fig. 15a. The poor model fit over much of the 4F data is due to the extrapolation beyond the range of n modeled. The 3F and 4F models provided very similar model fits in terms of prediction accuracy and the nature of the residuals, with the poorest prediction found at low fan speeds, which was encountered in the 4F case at low η and low U. The 3F model offered better prediction results than the 4F model with the OFAT validation data. The modeling results for the 3F case are given in Tables 16 and 17, with the response surface shown in Fig. 15b across J_x and M_{tip} with $J_z = 0$. A larger M_{tip} and a smaller J_x, which correspond to a higher fan speed and a lower freestream velocity, show a larger C_T response, as expected.

Table 16 Thrust coefficient model parameter estimates for 3F model

Term	$\hat{\theta}$	$s(\hat{\theta})$	% Error
C_{T_0}	1.248×10^{0}	1.027×10^{-3}	0.1
$C_{T_{J_x}}$	-9.675×10^{-1}	8.847×10^{-3}	0.9
$C_{T_{J_z}}$	-1.164×10^{-1}	1.230×10^{-2}	10.6
$C_{T_{J_x M_{\text{tip}}}}$	3.700×10^{-1}	6.936×10^{-2}	18.7
$C_{T_{J_x^2 M_{\text{tip}}}}$	1.372×10^{0}	1.900×10^{-1}	13.9

Table 17 3F thrust coefficient modeling and validation metrics

	R^2	NRMSE (%)
Model	0.999	0.802
Validation	0.999	0.753

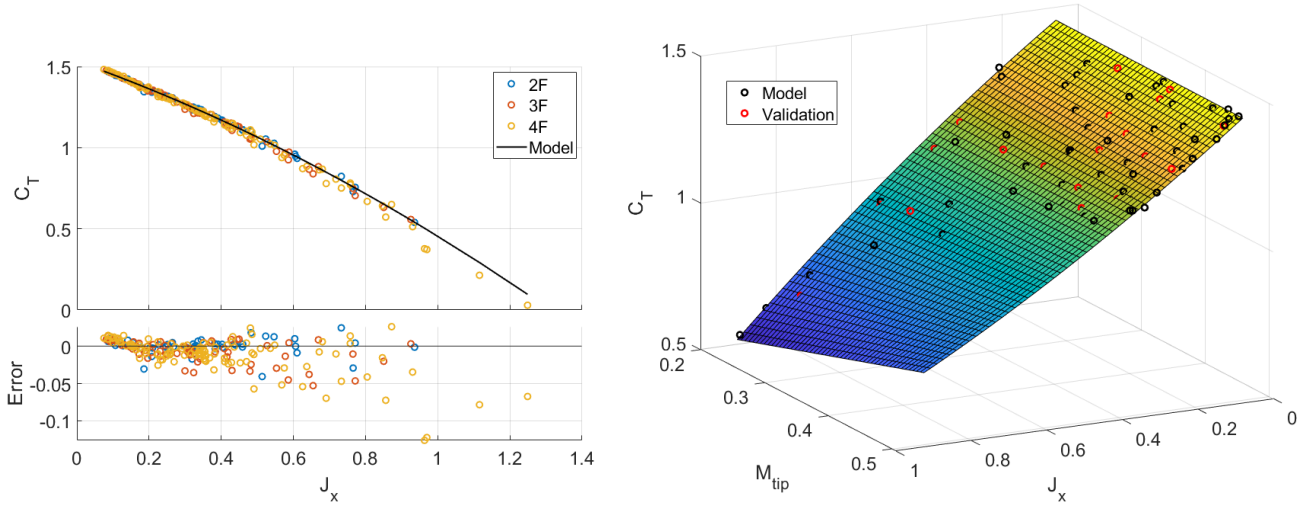

(a) Model fit for 2F model

(b) Response surface for 3F model with $J_z = 0$

Fig. 15 Thrust coefficient modeling results.

G. Power Model

A dimensional power model was developed to predict the DC power recorded from the power supply that was required to run the fan at a certain speed n. This dimensional model was selected over a more traditional C_p form because the EDF OGVs effectively zeroed the net torque measured, and an independent measurement of the motor torque was not available for C_p calculations. A constant voltage was set by the power supply at each test point, while the current draw was dependent on n.

The OFAT data in Fig. 5f show that the total power required is maximized in wind-off conditions, with a small reduction as a function of increasing $\bar{q}$. For this reason, the 2F wind-off power model did not extrapolate well, and the wind-on data were required to develop the power consumption model.

Similar to the approach in Section VI.F, the DOE 2F, 3F, and 4F data sets were used to develop separate power models, with the predictive capabilities compared to one another. Using each of these data sets, two separate approaches were taken to develop a power model: dimensional terms, $P = f(n, \bar{q}, i_p)$, and nondimensional terms, $P = f(J, M_{\text{tip}})$. Across both sets of model terms, the models developed provided a similar model fit, so the nondimensional model terms were chosen, with the model structure selected as

$$P = P_0 + P_J J + P_{M_{\text{tip}}} M_{\text{tip}} + P_{JM_{\text{tip}}} J M_{\text{tip}} + P_{M_{\text{tip}}^2} M_{\text{tip}}^2 + P_{M_{\text{tip}}^3} M_{\text{tip}}^3 \tag{15}$$

When the 2F and 3F models were tested on the 4F data, a small bias was apparent, as was the case when the 4F model was used to predict the 2F and 3F test points.

The response surface for the model built from the 3F data set is shown in Fig. 16, with the parameter estimates in Table 18 and the model fit metrics in Table 19. A larger M_{tip} and a smaller J, corresponding to a higher fan speed and a lower freestream velocity, cause a larger power draw, as expected.

Table 18 Parameter estimates for 3F power model

Term	$\hat{\theta}$	$s(\hat{\theta})$	% Error
P_0	2.552×10^{0}	4.349×10^{-3}	0.2
P_J	-2.934×10^{-1}	2.066×10^{-2}	7.0
$P_{M_{\text{tip}}}$	2.015×10^{1}	8.988×10^{-2}	0.4
$P_{JM_{\text{tip}}}$	-1.566×10^{0}	1.724×10^{-1}	11.0
$P_{M_{\text{tip}}^2}$	5.459×10^{1}	4.100×10^{-1}	0.8
$P_{M_{\text{tip}}^3}$	5.254×10^{1}	5.149×10^{0}	9.8

Table 19 3F power modeling and validation metrics

	R^2	NRMSE (%)
Model	1.000	0.374
Validation	1.000	0.388

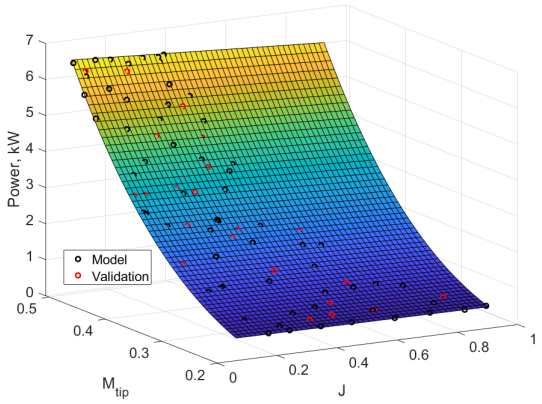

Fig. 16 Response surface for 3F power model.

VII. Thermal Aspects

Although thermal management was not a focal point of this work, and was addressed in concurrent 25% scale vehicle EDF testing [38], motor and ESC temperatures were monitored throughout the wind-off and wind-on testing to protect the test hardware and to ensure the maximum recommended temperature limits were not exceeded.

The motor is housed in a heat sink embedded in the EDF, as shown in Fig. 3, which covers most of the motor housing and facilitates heat dissipation. A maximum temperature of 176°F (80°C) is recommended for a BLDC motor with neodymium magnets to avoid demagnetization and permanent losses in performance. The motor temperature was monitored in real time during testing with a K-type thermocouple fixed to the outer motor housing behind the heat

sink. It was challenging to attain a seal over the thermocouple in the high speed fan efflux to provide reliable real-time readings when the fan was running; however, the time-averaged results appeared reasonable, and the thermocouple provided useful real-time data after the fan was stopped following each run, when temperature could be monitored prior to beginning a subsequent run. A Forward Looking Infrared (FLIR) thermal camera was also focused on the motor to provide a temperature distribution in real time, which was displayed on a monitor. A handheld IR thermometer was used between runs to check the motor temperature and validate the other measurements. The motor is automatically cooled with the air flow exiting the fan, as well as with the tunnel freestream velocity, so motor thermal management was not limiting during these tests. The test section started around 55°F throughout the test, which was also helpful in thermal management. Following each run, the measured motor temperature did not exceed 110°F.

The ESC was mounted to the sting normal to the freestream velocity (at $i_p = 0$) to maximize exposure to air flow, as shown in Fig. 4a, which was critical for extended use without alternative cooling. An internal thermocouple measured the ESC temperature, and these data were transmitted and monitored in real time. According to the manufacturer, the maximum continuous ESC temperature rating was 203°F (95°C), and a user-specified auto-shutoff feature could allow the ESC to shut down before a specified maximum temperature is reached. Real-time strip charts displayed rapid change in ESC temperature with changes in current draw, particularly in wind-off conditions. During OFAT runs, the current draw progressively increased with each new data point, which caused a sharp rise in temperature across the duration of the run, as shown in Fig. 17a. By the nature of the DOE designs, these runs were much better managed thermally since the ESC was allowed to cool down at lower fan speeds because current draw varied in both directions, as seen in Fig. 17b. During the built-in pauses for the HTC factors in the DOE runs, the fan was brought to idle to allow cooling before the run was resumed. This was an effective means of keeping the ESC temperature below 110°F throughout the test. The wind-off runs made it more difficult to manage the ESC temperature, but air cooling provided by a standard room fan placed near the ESC was helpful for any extended run duration.

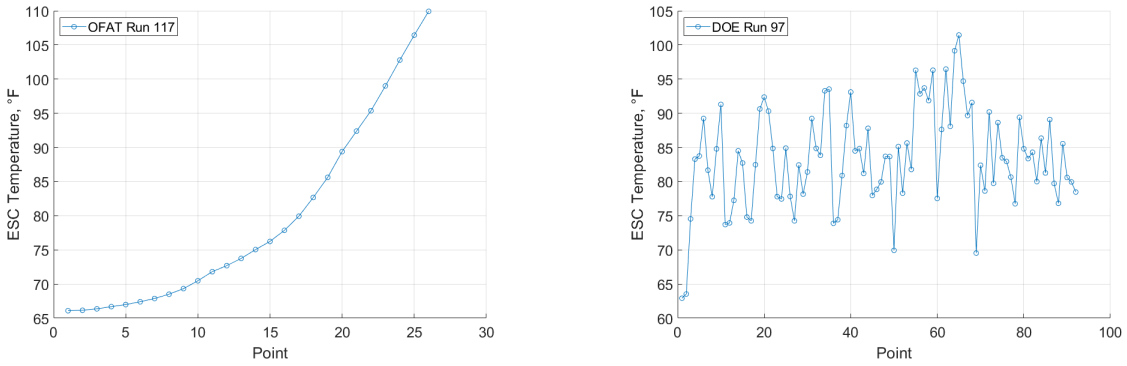

(a) ESC temperature during wind-off OFAT run

(b) ESC temperature during wind-on DOE run

Fig. 17 ESC temperature monitored during the test.

VIII. EDF Assessment for SUSAN 25% Scale Vehicle

The EDF v1 characterization and model development in this work was intended to evaluate the performance of the COTS fan, motor, and ESC for the SUSAN 25% scale vehicle. Each of the components performed reliably and consistently, and the EDF produced close to the thrust goal specified in Sec. IV.A within the power constraints, with the extrapolated thrust meeting the prescribed target at 7 kW of power. The measured static thrust compared well with manufacturer predictions; however, the power required was high compared to a similarly sized EDF [39]. With 8.5 kW of power available for each EDF, an alternative motor can also be selected to run this (or another) EDF to higher speeds and thrust values. This could provide recovery opportunities due to loss of fan failure cases without sacrificing the total thrust produced, or allow for additional flexibility for thrust-based control. Finally, the COTS inlet ring tested in this work is not representative of the mailslot housing envisioned for the SUSAN vehicle and pictured in Fig. 1, so the thrust produced will be different after the design and integration of the nacelles, as seen in Ref. [38].

The EDF performance for wind-on conditions was also evaluated based on the expected flight profile for the SUSAN 25% scale vehicle. Preliminary aerodynamic predictions stipulate a vehicle cruise velocity of 300 ft/s at 10,000 ft, while data were collected in the 12-Foot Low-Speed Tunnel up to 72 ft/s. Figure 18 shows the thrust and power model

predictions across several freestream velocities up to the cruise condition, with the extrapolated results designated in the legend with a "*". The thrust predictions show that the EDF can accelerate up to the cruise velocity, with some remaining thrust at high fan speed to accelerate beyond 300 ft/s. The power results show a moderate reduction in power required to operate as the freestream velocity increases. Because the results are scaled with J, the range of J that was tested and modeled is shown in the gray shaded region. Although no data were obtained for a large portion of the range shown, many of these test points are not producing positive thrust, and are thus not relevant flight conditions. The EDF v1 was only tested up to a limited range of freestream velocity, but given the scalability of the results with advance ratio, and that the cruise velocity of the SUSAN 25% scale vehicle remains within the incompressible flow regime, these results are used to predict that the EDF v1 is a suitable DEP unit for the flight vehicle.

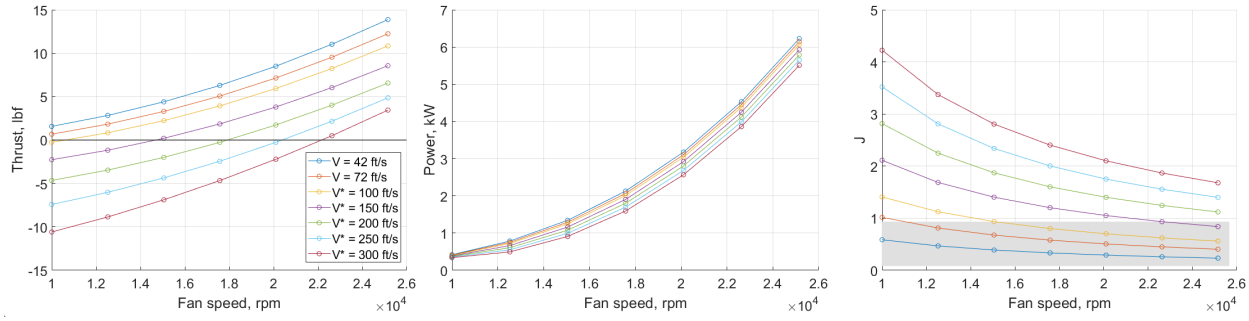

Fig. 18 Model predictions across the flight envelope.

IX. Conclusions

This paper described the process and results of characterizing a COTS EDF for the SUSAN 25% scale research vehicle. The EDF was tested in wind-off and wind-on conditions across four factors, including PWM input command, operating voltage, dynamic pressure, and incidence angle. A series of OFAT runs was first performed for design space exploration and general insight into modeling expectations, and then a set of DOE runs was completed to efficiently collect data across the test factors. A bracket drag model was developed to remove the drag effect of the EDF bracket structure, and then select runs were used to develop static motor, dynamic motor, fan thrust, and power consumption models. Each of these models was evaluated with validation data not used in the modeling process, and demonstrated excellent prediction capabilities.

The SUSAN concept is a hybrid electric commercial transport aircraft that provides most of the thrust through electrically driven propulsors along the wings instead of with traditional jet engines. This next generation vehicle design offers reduced emissions and improved sustainability, along with the opportunity to leverage the resulting PAI for control purposes. The isolated EDF characterization, modeling, and analysis in this work is an important step toward selecting a suitable EDF for the 25% scale vehicle that can fulfill the flight requirements and provide these benefits. Future work related to the SUSAN EDF development and characterization will extend beyond a single EDF to investigate the propulsor-propulsor and aero-propulsive interactions of several EDFs along a wing to better understand how the DEP will perform in flight.

Acknowledgments

This paper is based upon work supported by the NASA Aeronautics Research Mission Directorate (ARMD) Convergent Aeronautics Solutions (CAS) project. The efforts and contributions of several individuals are gratefully acknowledged for participating in the development and execution of these experiments, including Bruce Owens, George Altamirano, David North, Ronald Busan, Wes O'Neal, Earl Harris, Rick Thorpe, Clinton Duncan, and Lee Pollard.

References

[1] Welstead, J. R., and Felder, J. L., "Conceptual Design of a Single-Aisle Turboelectric Commercial Transport with Fuselage Boundary Layer Ingestion," *54th AIAA Aerospace Sciences Meeting,* AIAA Paper 2016-1027, January 2016. https://doi.org/10.2514/6.2016-1027.

[2] Goldberg, C., Nalianda, D., Pilidis, P., and Singh, R., "Economic Viability Assessment of NASA's Blended Wing Body N3-X Aircraft," *53rd AIAA/SAE/ASEE Joint Propulsion Conference,* AIAA Paper 2017-4604, July 2017. https://doi.org/10.2514/6.2017-4604.

[3] Jansen, R. H., Kiris, C. C., Chau, T., Machado, L. M., Duensing, J. C., Mirhashemi, A., Chapman, J., French, B. D., Miller, L., Litt, J. S., and Denham, C. L., "Subsonic Single Aft Engine (SUSAN) Transport Aircraft Concept and Trade Space Exploration," *AIAA SciTech 2022 Forum,* AIAA Paper 2022-2179, January 2022. https://doi.org/10.2514/6.2022-2179.

[4] Jansen, R. H., Kiris, C. C., Chau, T., Machado, L. G., Dever, T., Litt, J. S., Arthur, J. J., Lynde, M. N., Chapman, J. W., Kratz, J. L., and Turner, M. G., "Update on SUbsonic Single Aft eNgine (SUSAN) Electrofan Trade Space Exploration," *33rd Congress of the International Council of the Aeronautical Sciences (ICAS)*, September 2022.

[5] Lee, B. J., and Liou, M. F., "Conceptual Design of Propulsors for the SUSAN Electro-fan Aircraft," *AIAA SciTech 2022 Forum,* AIAA Paper 2022-2305, January 2022. https://doi.org/10.2514/6.2022-2305.

[6] Lynde, M. N., Campbell, R. L., and Hiller, B. R., "A Design Exploration of Natural Laminar Flow Applications for the SUSAN Electrofan Concept," *AIAA SciTech 2022 Forum,* AIAA Paper 2022-2303, January 2022. https://doi.org/10.2514/6.2022-2303.

[7] Chau, T., Kenway, G., and Kiris, C. C., "Conceptual Exploration of Aircraft Configurations for the SUSAN Electrofan," *AIAA SciTech 2022 Forum,* AIAA Paper 2022-2181, January 2022. https://doi.org/10.2514/6.2022-2181.

[8] Machado, L. M., Chau, T., Kenway, G. K., Duensing, J. C., and Kiris, C. C., "High-Fidelity Aerodynamic Analysis and Optimization of the SUSAN Electrofan Concept," *AIAA SciTech 2022 Forum,* AIAA Paper 2022-2304, January 2022. https://doi.org/10.2514/6.2022-2304.

[9] Yaros, S. F., Sexstone, M. G., Huebner, L. D., Lamar, J. E., McKinley Jr, R. E., Torres, A. O., Burley, C. L., Scott, R. C., and Small, W. J., "Synergistic Airframe-Propulsion Interactions and Integrations: A White Paper Prepared by the 1996-1997 Langley Aeronautics Technical Committee," NASA Langley Research Center, NASA TM 1998-207644, March 1998. https://ntrs.nasa.gov/citations/19980055126.

[10] Kim, H., Perry, A. T., and Ansell, P. J., "A Review of Distributed Electric Propulsion Concepts for Air Vehicle Technology," NASA Langley Research Center, NASA TM 1998-207644, March 1998. https://ntrs.nasa.gov/citations/19980055126.

[11] Koch, L. D., "Predicting the Inflow Distortion Tone Noise of the NASA Glenn Advanced Noise Control Fan with a Combined Quadrupole-Dipole Model," *18th AIAA/CEAS Aeroacoustics Conference*, June 2012. https://doi.org/10.2514/6.2012-2196.

[12] Provenza, A. J., Duffy, K. P., and Bakhle, M. A., "Aeromechanical response of a distortion-tolerant boundary layer ingesting fan," *Journal of Engineering for Gas Turbines and Power*, Vol. 141, No. 1, 2019, p. 011011. https://doi.org/10.1115/1.4040739.

[13] Foster, J. V., and Hartman, D., "High-Fidelity Multi-Rotor Unmanned Aircraft System (UAS) Simulation Development for Trajectory Prediction Under Off-Nominal Flight Dynamics," *17th AIAA Aviation Technology, Integration, and Operations Conference,* AIAA Paper 2017-3271, June 2017. https://doi.org/10.2514/6.2017-3271.

[14] Simmons, B. M., "System Identification for Propellers at High Incidence Angles," *Journal of Aircraft*, Vol. 58, No. 6, 2021, pp. 1336–1350. https://doi.org/10.2514/1.C036329.

[15] Simmons, B. M., "Efficient Variable-Pitch Propeller Aerodynamic Model Development for Vectored-Thrust eVTOL Aircraft," *AIAA Aviation 2022 Forum,* AIAA Paper 2022-3817, June 2022. https://doi.org/10.2514/6.2022-3817.

[16] Busan, R. C., Rothhaar, P. M., Croom, M. A., Murphy, P. C., Grafton, S. B., and O'Neal, A. W., "Enabling Advanced Wind-Tunnel Research Methods Using the NASA Langley 12-Foot Low Speed Tunnel," *14th AIAA Aviation Technology, Integration, and Operations Conference,* AIAA Paper 2014-3000, June 2014. https://doi.org/10.2514/6.2014-3000.

[17] Murphy, P. C., Hatke, D. B., Aubuchon, V. V., Weinstein, R., and Busan, R. C., "Preliminary Steps in Developing Rapid Aero Modeling Technology," *AIAA SciTech Conference,* AIAA Paper 2020-0764, January 2020. https://doi.org/10.2514/6.2020-0764.

[18] Murphy, P. C., and Landman, D., "Experiment Design for Complex VTOL Aircraft with Distributed Propulsion and Tilt Wing," *AIAA SciTech 2015 Forum,* AIAA Paper 2015-0017, January 2015. https://doi.org/10.2514/6.2015-0017.

[19] Simmons, B. M., and Murphy, P. C., "Aero-Propulsive Modeling for Tilt-Wing, Distributed Propulsion Aircraft Using Wind Tunnel Data," *Journal of Aircraft*, Vol. 59, No. 5, 2022, pp. 1162–1178. https://doi.org/10.2514/1.C036351.

[20] Rutkowski, M., and Krusz, W., "Design and Analysis of Ducted Fan for Multi-Rotor VTOL UAV," *PhD Interdisciplinary Journal Politechnike Gdanska*, 2013, pp. 149–155. https://doi.org/10.2514/1.C036351.

[21] Hughes, C., "Aerodynamic Performance of Scale-Model Turbofan Outlet Guide Vanes Designed for Low Noise," *40th AIAA Aerospace Sciences Meeting and Exhibit,* AIAA Paper 2002-0374, January 2002. https://doi.org/10.2514/6.2002-374.

[22] Harris, F. D., "Hover Performance of Isolated Proprotors and Propellers - Experimental Data," NASA CR 219486, 2017.

[23] Mort, K. W., and Gamse, B., "A Wind-Tunnel Investigation of a 7-Foot-Diameter Ducted Propeller," NASA-TN-D-4142, 1967.

[24] Abrego, A. I., and Bulaga, R. W., "A Wind-Tunnel Investigation of a 7-Foot-Diameter Ducted Propeller," *American Helicopter Society Aerodynamics, Acoustics and Test and Evaluation Technical Specialists Meeting*, 2002.

[25] "737 MAX Airplane Characteristics for Airport Planning," `https://www.boeing.com/resources/boeingdotcom/commercial/airports/acaps/737MAX_RevH.pdf`, Boeing. Retrieved: 22 November 2023.

[26] "EASA Type Certificate Data Sheet for LEAP-1B Series Engine," `https://www.easa.europa.eu/en/document-library/type-certificates/engine-cs-e/easae115-leap-1b-series-engines`, EASA. Retrieved: 22 November 2023.

[27] Lee, B. J., and Liou, M. F., "Conceptual Design of Propulsors for the SUSAN Electro-fan Aircraft," *AIAA SciTech 2022 Forum,* AIAA Paper 2022-2305, January 2022. https://doi.org/10.2514/6.2022-2305.

[28] Montgomery, D. C., *Design And Analysis of Experiments*, 8th ed., John Wiley & Sons, Inc., Hoboken, NJ, 2013.

[29] Myers, R. H., Montgomery, D. C., and Anderson-Cook, C. M., *Response Surface Methodology: Process and Product Optimization Using Designed Experiments*, 4th ed., John Wiley & Sons, Hoboken, NJ, 2016.

[30] Jones, B., and Nachtsheim, C. J., "Split-Plot Designs: What, Why, and How," *Journal of Quality Technology*, Vol. 41, No. 4, 2009, pp. 340–361. https://doi.org/10.1080/00224065.2009.11917790.

[31] Cortes, L. A., Simpson, J. R., and Parker, P. A., "Response surface split-plot designs: A literature review," *Quality and Reliability Engineering International*, Vol. 34, No. 7, 2018, pp. 1374–1389. https://doi.org/10.1002/qre.2350.

[32] "Design-Expert®," Version 13, Stat-Ease, Inc., https://www.statease.com/software/design-expert/, Accessed 11 May 2022.

[33] Simmons, B. M., "Efficient Variable-Pitch Propeller Aerodynamic Model Development for Vectored-Thrust eVTOL Aircraft," *AIAA AVIATION 2022 Forum*, AIAA Paper 2022-3817, June 2022. https://doi.org/10.2514/6.2022-3817.

[34] Morelli, E. A., and Klein, V., *Aircraft System Identification: Theory and Practice*, 2nd ed., Sunflyte Enterprises, Williamsburg, VA, 2016.

[35] Morelli, E. A., "Global Nonlinear Aerodynamic Modeling Using Multivariate Orthogonal Functions," *Journal of Aircraft*, Vol. 32, No. 2, 1995, pp. 270–277. https://doi.org/10.2514/3.46712.

[36] Goos, P., and Jones, B., *Optimal Design of Experiments*, John Wiley & Sons, West Sussex, United Kingdom, 2011.

[37] Simmons, B. M., "Evaluation of Response Surface Experiment Designs for Distributed Propulsion Aircraft Aero-Propulsive Modeling," *AIAA SciTech 2023 Forum*, AIAA Paper 2023-2251, January 2023. https://doi.org/10.2514/6.2023-2251.

[38] Asfoor, F., Stalcup, E., and Koch, L. D., "NASA's Quiet Electric ENgines (QUEEN): Summary of the QUEEN V2 Test," *AIAA SciTech 2024 Forum*, January 2024 (to be published).

[39] Darrah, D., Eppler, J., Liu, W., and Anemaat, W. A., "Electric Ducted Fan Design and Testing for High Performance UAV Integration," *AIAA SciTech 2020 Forum,* AIAA Paper 2020-0017, January 2020. https://doi.org/10.2514/6.2020-0017.